Structural Analysis of Fiber-Reinforced Metallic Rocket Motor Cases Using Finite-Element and Photoelastic Techniques

J. Margetson* and A. Groves†
Royal Armament Research and Development Establishment, Buckinghamshire, England
and
T. E. Thorpe‡
University of Manchester, Manchester, England

Stress analysis procedures are presented for fiber-reinforced metallic rocket motor cases using finite-element and photoelastic techniques. These techniques enable analyses of the initial winding process, inertia, and pressurization due to firing to be performed. Certain simplifications and assumptions are introduced to resolve the complicating effects of the fiber overwind and the in-flight loadings. A comparison of the two methods for a typical motor is made.

Nomenclature

A	= defined by Eq. (4)
E	= Young's modulus
$F_i(A,n)$	= defined by Eq. (3)
n	= number of applied fiber layers
p	= internal pressure
p_b, p_{bw}, p_{bp}	= interface pressure, interface pressure component due to winding, and interface pressure component due to pressurization
R	= mean radius
R_i, R_b, R_o	= internal radius, fiber/case interface radius, and outer radius of overwound motor
R_e	= effective radius of throat insert
t	= thickness
ϵ	= strain
Δ	= change
σ	= stress
ν	= Poisson's ratio

Subscripts

c	= case
f	= fiber
p	= pressurization
w	= winding
z	= axial direction
θ	= circumferential direction

Superscripts

(i,n)	= ith fiber layer of n fiber layers
(n)	= n fiber layers

I. Introduction

THE selection of materials with high specific strengths, i.e., a high ratio of ultimate tensile strength to specific gravity, is an important feature in the design of rocket motor cases. Maraging steel, for example, with an ultimate tensile strength of 2200 MPa and a specific gravity of 8, is one of the highest specific strength materials suitable for "single" material designs. Attempts to use even higher-strength steels have, however, generated serious quality assurance problems associated, for instance, with their reduced ductility, and some motors have failed in a brittle manner.

Alternatively, with the choice of suitable constituent materials, composite rocket motor cases can be manufactured with specific strengths exceeding that of any homogeneous design. A lightweight, load-bearing, aluminum tube, circumferentially reinforced with a high-strength polyamide fiber, is a particular example. Furthermore, if the fiber overwind is applied under tension, the case is put into compression. This defers the onset of tensile stresses and thereby effectively increases the firing pressure of the motor. In spite of these advantages, prestraining has potential drawbacks. For example, experimental tests have shown that the strength and modulus of the fiber are reduced with prolonged periods of loading. Nevertheless, provided that adequate allowances are made for such degradations at the design stage, the considerable increase in the effective strength usually outweighs these drawbacks.

In the past, the stress analysis of fiber-reinforced metallic rocket motor cases has been performed empirically,[1-3] but in recent years, the authors have been involved in the development of theoretical stressing procedures.[4-8] This work has involved analyses of the initial winding process for both constant and variable winding strains, temperature excursions about the ambient winding temperature, and the response of the motor when subjected to its firing pressure.

A typical solid-propellant rocket motor is shown in Fig. 1. The solid-propellant charge, shown star-shaped to the rear of the motor and cylinder-shaped to the front in the figure, provides the propulsion and in this particular motor is bonded to a Kevlar overwrapped aluminum motor case. The intermediate liner acts as a thermal insulator and contains a stress-relieving device (a "booted" section) designed to prevent the propellant from debonding from the case. The blast pipe (an insulated fiber overwrapped aluminum cylinder) connects the rear end of the motor case to the nozzle assembly. In the nozzle assembly, the hot exhaust gases are passed through a throat insert (made from graphite, tungsten, carbon/carbon, etc.) and then expanded through a heat-resistant expansion cone.

For the thin-walled cylindrical portion of the motor, analytical stress solutions have been developed, whereas for

Received May 8, 1986; revision received Feb. 9, 1987.

*Head of Structural Analysis Section.
†Research Scientist.
‡Lecturer in Mechanical Engineering, Simon Engineering Laboratories.

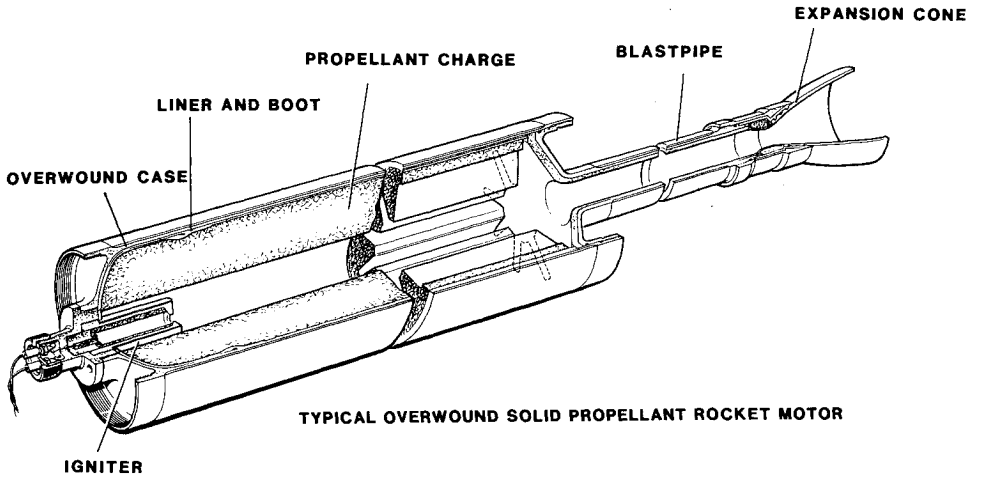

Fig. 1 Typical overwound solid-propellant rocket motor.

the thicker and geometrically more complex regions of the motor, finite-element procedures have been applied. Photoelastic stress analysis procedures have also been developed for fiber-reinforced rocket motor cases[9] so that the three-dimensional effects of the geometry, which cannot be readily analyzed using the theoretical procedures, can be studied. In this paper, the theoretical and photoelastic techniques that have been used to analyze fiber-reinforced metallic rocket motor cases are reviewed, and their respective stress solutions are compared for a typical motor.

II. Thin-Walled Section Analysis

A. Overwinding Analysis

When n layers of fiber overwind are wound circumferentially at an initial winding strain ϵ_w onto a metal case of mean radius R, the case contracts radially due to the external pressure of the overwind and is thereby put in compression. In the absence of internal pressure, the axial stress is zero, and assuming that the radial contraction of the motor due to the application of each fiber layer is uniform throughout the structure, it has been shown[5] that the elastic prestress in the ith fiber layer and the case, $\sigma_{\theta f}^{(i,n)}$ and $\sigma_{\theta c}^{(n)}$, respectively, are given by

$$\sigma_{\theta f}^{(i,n)} = E_f \epsilon_w [1 - AF_i(A,n)], \quad i = 1,2,\ldots,n \tag{1}$$

$$\sigma_{\theta c}^{(n)} = -E_c \epsilon_w A F_1(A,n) \tag{2}$$

where

$$F_i(A,n) = \sum_{j=i}^{n} \frac{1}{1+Aj} \tag{3}$$

with the stiffness parameter A denoting

$$A = \frac{E_f t_f}{E_c t_c} \tag{4}$$

In these equations, the quantities E_f and E_c are Young's modulus values for the fibers and case, respectively, t_f is the effective thickness of a single fiber layer, and t_c is the wall thickness of the metallic case.

For ease of computation, it is convenient to approximate the summation term [i.e, $F_i(A,n)$] appearing in Eqs. (1) and (2) by an analytical expression. Using the Euler-Maclaurin formula[10] and neglecting all first-order and greater terms, Eq. (3) modifies to

$$F_i(A,n) = \frac{1}{A} \ln\left[\frac{1+An}{1+Ai}\right] + \frac{1}{2(1+An)} + \frac{1}{2(1+Ai)} \tag{5}$$

Detailed computations have shown that for typical A values (i.e., $A \ll 1$), the errors associated with this approximation are very small (on the order 0.05%).

Having derived the stresses in the fibers and the case, the corresponding elastic strains follow from the uniaxial Hookean stress-strain relationship.

B. Pressurization Analysis

When the rocket motor case is subjected to its firing pressure, it is a requirement that the motor must withstand all in-flight loads without failure or excessive deformation. Although these in-flight loads may contain components due to inertia and aeroheat, the dominant load will usually be the firing pressure.

In the overwinding analysis, the axial stress was zero. However, when the motor is subjected to its firing pressure, the axial stress will, in general, be nonzero and is given by

$$\sigma_{zcp} = p \frac{(R^2 - R_e^2)}{2Rt_c} \tag{6}$$

where R_e is the effective internal radius[5] of the throat insert, taking into account the nonuniform pressure distribution acting over the nozzle region. When an allowance for inertia effects is included, R_e will contain an additional component due to the axially varying inertia force.

The circumferential stresses in the fibers and the case are also modified when the motor is subjected to its firing pressure. It can be shown from a previous analysis[5] that the modified elastic circumferential stresses in the ith fiber layer and the case, $\sigma_{\theta fp}^{(i,n)}$ and $\sigma_{\theta cp}^{(n)}$, respectively, are given by

$$\sigma_{\theta fp}^{(i,n)} = E_f \epsilon_w [1 - AF_i(A,n)] + \frac{pRA}{t_f(1+nA)}\left[1 - \frac{\nu_c}{2}\left(1 - \frac{R_e^2}{R^2}\right)\right], \quad i = 1,2,\ldots,n \tag{7}$$

$$\sigma_{\theta cp}^{(n)} = -E_c \epsilon_w F_1(A,n) + \frac{pR}{t_c(1+nA)}\left[1 + \frac{n\nu_c A}{2}\left(1 - \frac{R_e^2}{R^2}\right)\right] \tag{8}$$

where ν_c denotes the Poisson's ratio of the metallic case and p is the firing pressure. As before, having obtained the stresses, the elastic strains follow from the Hookean stress-strain relations.

III. Thick-Walled Section Analysis

In the preceding section, simple analytical stress solutions were presented for the thin-walled sections of the motor, which are remote from the constraining influence of the end closures. For the thick-walled sections and geometrically complex regions of the case, such as the end closure and transition regions of the motor case into the blast pipe and nozzle assembly (see Fig. 1), a more sophisticated stress analysis approach is required.

For complex geometries, the required stress analysis can be performed either theoretically or experimentally. For a theoretical analysis, finite-element techniques have to be adopted, whereas for an experimental study, strain gauging or photoelastic procedures can be applied. For experimental studies, the photoelastic technique is usually preferred, since it provides stress information at both the surface and interior points of the structure. It also has the advantage of providing detailed information of the stress variations in the regions of high stress concentrations, taking into account full three-dimensional effects of the geometry.

The finite-element and photoelastic techniques are well documented[11,12] and are both capable of providing accurate stress predictions. However, the manner in which these techniques are applied to the overwound rocket motor case is not entirely straightforward due to the complicating effects of the fiber overwind and the in-flight loadings. Both methods of analysis are now discussed.

A. Finite-Element Analysis

For a rigorous stress analysis of the fiber-reinforced metallic rocket motor case, it is necessary to employ specialized finite-element programs that provide facilities for accurately modeling the reinforcing properties of the fiber overwind and the prestress produced during winding. Although such programs are under development, they are not yet available for use, and it has been necessary to develop an alternative, albeit approximate, solution procedure using existing finite-element programs. In this particular study, an in-house-developed axisymmetric finite-element code based on an eight-noded isoparametric element formulation, which incorporated pressurization and inertia loading facilities, was used for the stress analysis.

In the theory of finite-element stress analysis, there exists a technique known as substructuring, which enables the analysis of complex structures to be simplified. This technique involves the replacement of part of a structure by a set of equivalent forces or displacements applied to the interface boundary of the retained portion.[11] For the overwound motor, it follows, therefore, that the overwind can be removed and structurally represented by applying an external pressure, equal in magnitude to the interface pressure between the first fiber layer and the metal case, over the region previously occupied by the fiber overwind. The remaining structure, a homogeneous isotropic metal case, can then be analyzed by any conventional axisymmetric finite-element program.

At this stage, it would seem logical to evaluate the fiber/case interface pressure p_b by first calculating the circumferential stress $\sigma_{\theta cp}^{(n)}$ from Eq. (8) and then using the thin-walled cylinder equation to give

$$p_b = p - \frac{\sigma_{\theta cp}^{(n)} t_c}{R} \tag{9}$$

However, in situations where the interface pressure p_b and the applied internal pressure p are almost equal, it has been found from an error analysis for the circumferential stress (see Appendix A) that as p_b approaches p, a small error in the determination of p_b will lead to a large error in the circumferential stress calculation. Although Eq. (9) yields an interface pressure within a few percent of that predicted by the exact Lame equations,[15] serious errors were observed in the finite-element stress solutions (in excess of 25%) when this estimate of p_b was used. To ensure that accurate results are generated, it is vital that the more precise relationship based on the Lame equations (see Appendix A)

$$p_b = p\left\{\left[\frac{2R_i^2}{E_c(R_b^2 - R_i^2)} - \frac{\nu_c(R_i^2 - R_e^2)}{E_c(R_b^2 - R_i^2)}\right] \div \left[\frac{R_b^2 + R_i^2}{E_c(R_b^2 - R_i^2)} + \frac{R_o^2 + R_b^2}{E_f(R_o^2 - R_b^2)}\right]\right\} + \frac{E_c \epsilon_w A F_1(A,n) t_c}{R} \tag{10}$$

is used in the finite-element analysis, where R_i and R_b denote, respectively, the internal and interface radii of the metallic case and R_o is the external radius of the overwound motor, i.e., $R_b + nt_f$.

In this approximate analysis, the overwound section of the motor is divided into a series of cylinders, the lengths of which are selected to take into account the nonuniform axial stress variation due to inertia and possible variations in the total thickness of the fiber overwind and the case. For each cylinder, the quantity R_e appearing in Eq. (10) is calculated from Eq. (6) in terms of the axial stress. This axial stress consists of two components, one of which is proportional to the constant axially resolved integrated force due to the nonuniform internal pressure acting over the nozzle region, and one due to inertia, which is axially nonuniform. It should be noted that in the vicinity of the ends of the overwound section of the case, the cylinder approximation is not strictly valid, but experimental results indicate that this method of analysis provides a reasonable working model for this theoretical study (see Sec. IV).

Since R_e is derived from the axial stress distribution, it follows that the fiber/case interface pressure [see Eq. (10)] is a function of the stress state being calculated. The solution process is therefore iterative, requiring an initial approximation for R_e and hence the interface pressure for each cylinder, followed by a succession of finite-element stress analyses with R_e and the interface pressure being updated between each iteration.

An initial approximation for R_e for each cylinder can be obtained by performing a finite-element stress analysis of the motor with all in-flight loads present but with the presence of the overwind omitted. The derived axial stress solution is then used together with Eq. (6) to obtain the required R_e values with the corresponding interfacial pressure p_b following from Eq. (10).

Once the initial interface pressure has been calculated, the isotropic finite-element analysis can be performed, using, in this case, all in-flight loads together with the calculated interface pressures applied externally to the regions previously reinforced by the fiber overwind. An improved estimate for the axial stress is then obtained, and from this, a modified value for R_e for each cylinder is determined from Eq. (6). The updated interface pressures then follow from Eq. (10). The whole process is repeated until the difference between successive stress solutions is less than a few percent. Computations have shown that convergence is obtained within four or five iterations. This procedure is shown schematically in Fig. 2.

B. Photoelastic Analysis

To assess the analytical work presented in the previous sections and to model certain three-dimensional effects (slots and holes) which were beyond the scope of the axisymmetric analysis, the stress state in the overwound motor case was also determined experimentally using the three-dimensional "frozen-stress" photoelastic technique.[13,14] The models (twice full size) were machined from cast blanks of Araldite CT200, and a separate model was used for each form of loading (see next section). The results were then combined by simple superposition to obtain the final stress state. Each stress-frozen model was sliced in both the meridional and circumferential planes, and fringe readings were taken in a standard diffuse-light polariscope at the inner and outer edges of each slice. Standard techniques were used for material calibration, and the motor stresses were obtained by proportionate scaling as outlined in the following discussion. The approach for each of the three forms of loading studied is discussed next.

1. Inertia Loading

Stresses due to the inertia loadings resulting from 1) the rocket motor's own mass and 2) the fins were studied separately. The former were obtained from a model subjected to a simple deadweight axial loading (see Fig. 3). The inertia load at any transverse plane in the motor is equal to the product of the mass of that part of the motor between the plane and the outlet and its acceleration. In order to obtain the inertia stress at any particular transverse section of the motor, the model stresses were increased by a factor of four (to allow for model scale) and then by the ratio of the calculated inertia load at the section to the load applied to the model.

Stresses due to the fin loading were obtained from a model subjected to deadweight loads applied to metal strips fitted into each of the four fin slots nearest the nozzle outlet. Motor stresses were obtained by proportionate scaling.

2. Pressure Loading

The nonuniform internal pressure in the motor was simulated in the model by a hydrostatic pressure loading using a combination of glycerine and Wood's metal (a low-melting point alloy that is liquid at the stress-freezing temperature). The levels of the two "liquids" inside and outside the model (see Fig. 4) were such that a two-slope linearly varying pressure was obtained in the nozzle region of the motor and a constant pressure was obtained in the cylindrical portion. The relative densities of the liquids were such that, in relative terms, this pressure distribution was closely similar to that in the motor (Fig. 5). Motor stresses were obtained from model stresses by simple scaling.

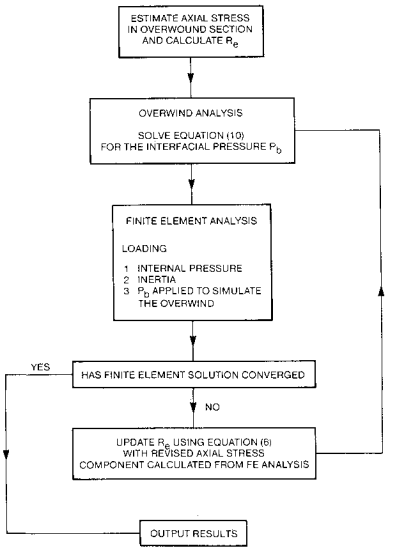

Fig. 2 Approximate finite-element solution procedure.

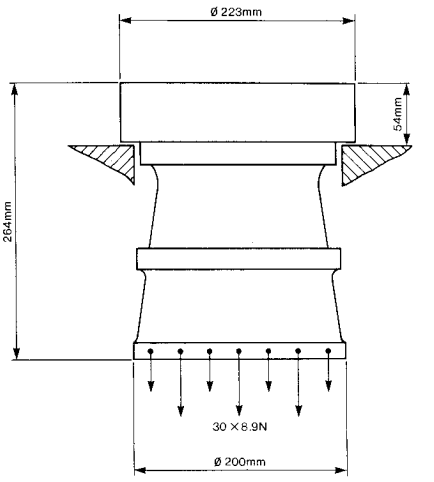

Fig. 3 Inertia loading simulation procedure.

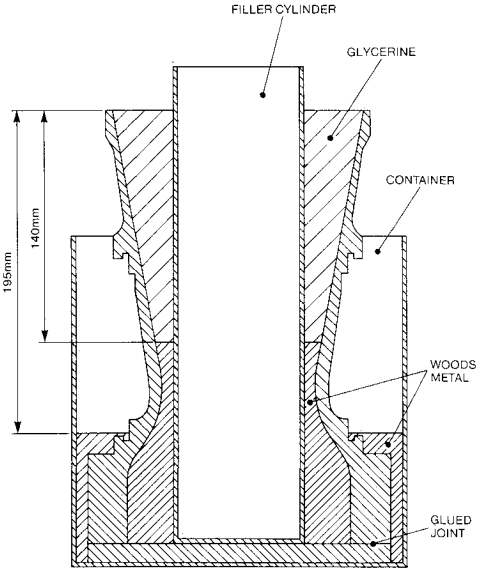

Fig. 4 Nonuniform pressure simulation procedure.

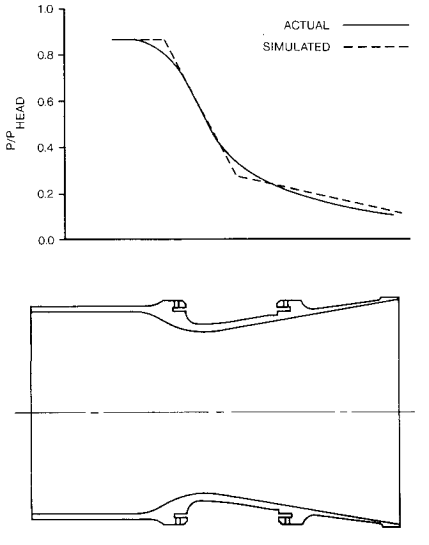

Fig. 5 Pressure distribution through nozzle.

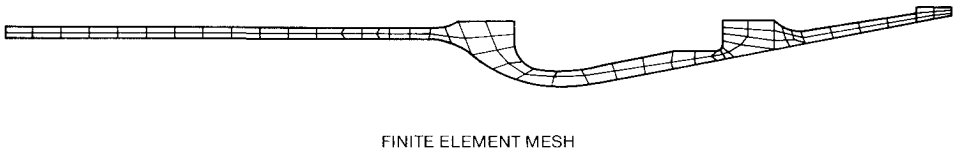

Fig. 6 Finite-element mesh.

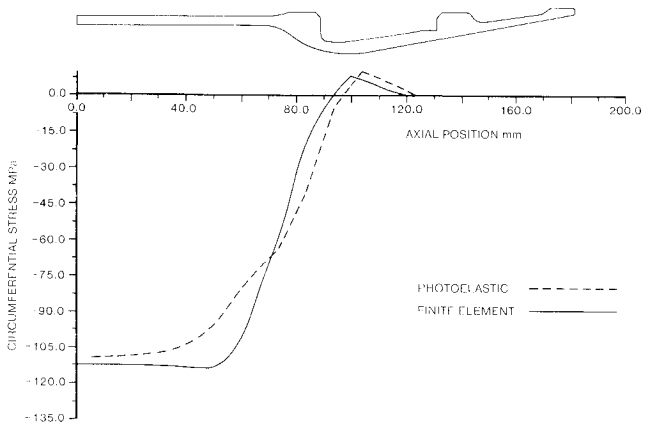

Fig. 7 Circumferential stress vs axial station: overwound state (inner surface).

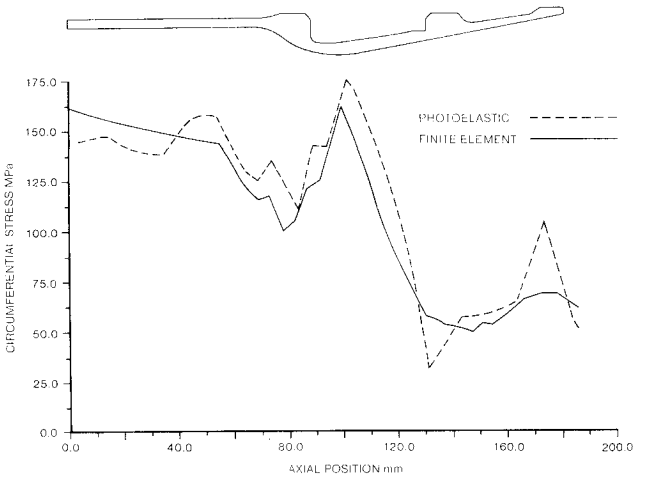

Fig. 9 Circumferential stress vs axial station: combined loading (inner surface).

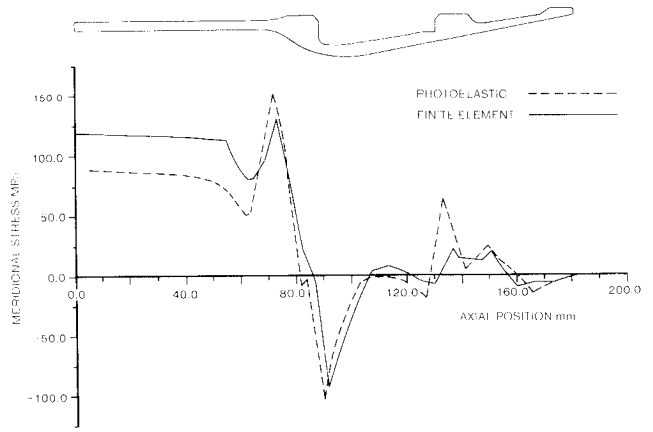

Fig. 8 Meridional stress vs axial station: inertia loading (inner surface).

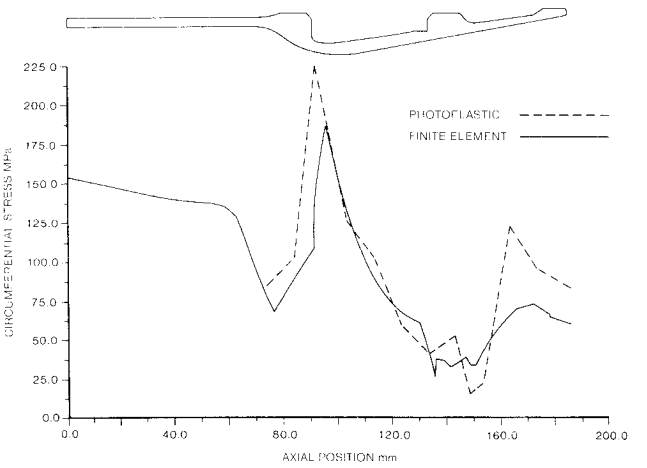

Fig. 10 Circumferential stress vs axial station: combined loading (outer surface).

3. Overwinding

The prestress resulting from the overwinding process was simulated by shrink-fitting a series of Araldite rings onto the parallel cylindrical section of the model. The ring/cylinder interference was chosen to give acceptable fringe orders in the stress-frozen model; the rings were heated to 135°C to allow them to be fitted onto the cylinder. An expression is available[5] for the mean circumferential stress produced in the cylinder in terms of the relevant motor variables. In obtaining the motor stresses from the model results, the model stresses were scaled by the ratio of the calculated mean circumferential stress in the motor to the observed mean circumferential stress in the cylindrical portion of the model.

IV. Comparison of Finite-Element and Photoelastic Stress Results

Finite-element and photoelastic results have been compared for a typical motor case using representative material property data and in-flight loads. A typical nonuniform pressure distribution derived from Bernoulli's equation for adiabatic isentropic flow acting on the inner surface of the motor and nozzle is shown by the solid line in Fig. 5.

Because of the complexities associated with the motor geometry and in-flight loadings, certain simplifying assumptions were introduced into the finite-element analysis. The fin slots and location holes, which could not be modeled by the axisymmetric finite-element program, were omitted and replaced by solid sections in the finite-element mesh. Furthermore, to model the influence of the fins, an element of representative mass was positioned adjacent to the fins' rear location point. The final finite-element mesh employed (see Fig. 6) represented a compromise between solution accuracy and computer storage. Saint Venant's principle was invoked, and the parallel section of the motor was truncated one diameter in length from the end of the overwound portion of the motor. A comparison between the finite-element and thin-walled cylinder solutions showed that the influence of the nozzle did not extend beyond that point.

The results of the finite-element and photoelastic stress analyses are presented in Figs. 7–12. Selected plots of the circumferential and meridional stress distributions at the inner and outer surfaces of the motor for the same cross section are illustrated. A plot of the deformed shape obtained from the finite-element analysis is also presented in Fig. 13.

In Figs. 7 and 8, the circumferential and meridional stresses are plotted, respectively, for the overwinding and inertia loading conditions. These two quantities represent the dominant stresses produced for the two load cases. In Fig. 7, where the circumferential stress distributions obtained from both analyses are plotted for the inner surface, the stress predictions are, in general, in good agreement. However, differences are observed for the region at the end of the overwound section, which is close to the nozzle inlet. In the finite-element analysis, the thin-walled cylinder equations were used to obtain the interface pressure p for this region, and consequently, "end effect" errors may have been introduced. This method of evaluating p_b is an intrinsic feature of the approximate finite-element procedure, and the introduction of these errors is unavoidable.

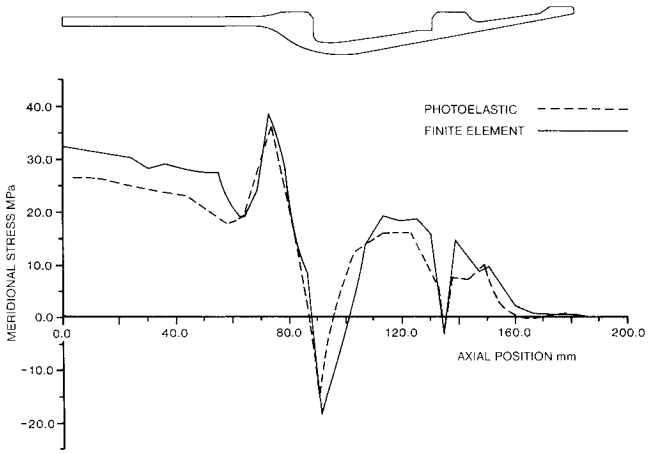

Fig. 11 Meridional stress vs axial station: combined loading (inner surface).

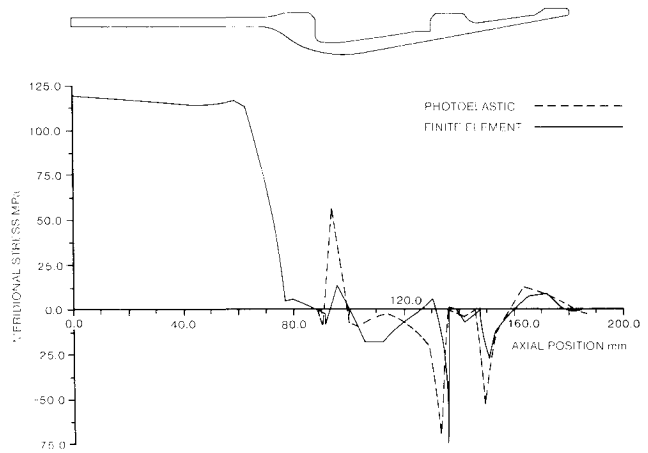

Fig. 12 Meridional stress vs axial station: combined loading (outer surface).

In Fig. 8, where meridional stress distributions at the inner surface of the rocket motor case are plotted for the inertia loading condition, it can be seen that the finite-element stress predictions are again in reasonable agreement with the photoelastic results. However, unexpected differences occurred in the thin-walled parallel section of the motor, and since the finite-element and analytical solutions are in close agreement, this difference has probably been introduced through a deficiency in the inertia modeling used in the photoelastic analysis.

In Figs. 9–12, both the meridional and circumferential stress distributions are plotted for both the inner and outer surfaces for the combined loading case, i.e., overwinding, inertia, and pressurization. Since the pressurization analysis is included in the combined loading analysis, a separate assessment of that loading case has not been presented. Again, there is good agreement between the finite-element and photoelastic results. However, the following points are worth noting:

1) In Figs. 9 and 10, where the circumferential stress distributions are plotted for the inner and outer surfaces, respectively, differences in the peak stresses are observed. These differences are attributable to the coarseness of the finite-element mesh employed adjacent to sudden changes in motor geometry and the three-dimensional effects of the fin slots and location holes included in the photoelastic analysis.

2) For combined loading conditions, there is also good agreement between the two stressing techniques for the prediction of the meridional stress distribution at the inner (see Fig. 11) and outer (see Fig. 12) surfaces. The differences present in the inertia analysis have been carried through to the combined loading analysis. The photoelastic predictions for the thin-walled section consequently differ slightly from that given by the finite-element solution.

3) Although the interface pressure between the first fiber layer and the case can be evaluated theoretically, it is nevertheless an empirically unknown quantity. Consequently, photoelastic stress solutions could not be obtained for the outer surface of the overwound portion of the motor.

V. Conclusions

Stress analysis procedures using the finite-element and photoelastic techniques for analyzing fiber-reinforced metallic rocket motor cases have been presented. These techniques enabled an analysis of the overwinding process,

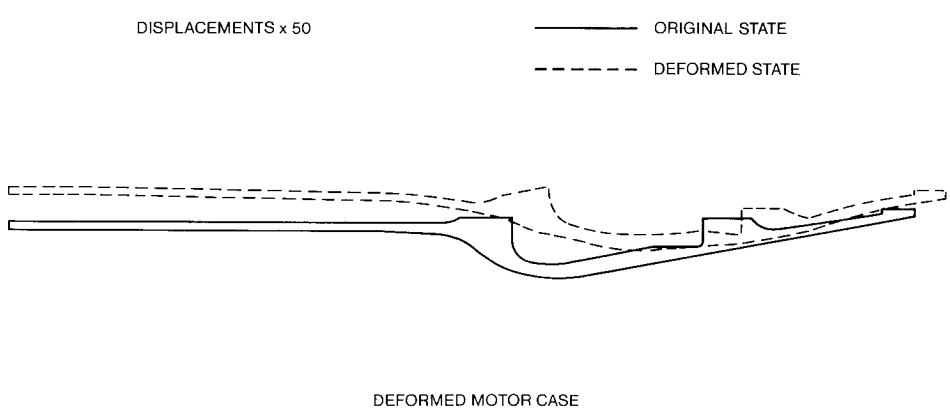

Fig. 13 Deformed motor case.

inertia, and pressurization due to firing to be performed. Certain simplifications and assumptions had to be introduced into both methods. When the two procedures were applied to the stress analysis of a typical overwound rocket motor case, reasonable agreement was achieved for all load cases studied.

Appendix A: Interface Pressure Calculation

The interface pressure p_b between the first fiber layer and the case consists of two components, one due to winding (p_{bw}) and one due to the application of the internal pressure (p_{bp}). The winding-induced component p_{bw} can be readily obtained from the prestress produced during winding $\sigma_{\theta c}^{(n)}$ through the thin-walled cylinder equations in the form

$$p_{bw} = \frac{-\sigma_{\theta c}^{(n)} t_c}{R} \tag{A1}$$

which, when using Eq. (2) to eliminate $\sigma_{\theta c}^{(n)}$, modifies to

$$p_{bw} = \frac{E_c \epsilon_w A F_1(A,n) t_c}{R} \tag{A2}$$

In principle, it would also seem admissible to use the thin-walled cylinder approximations to calculate the pressure-induced interface pressure component p_{bp} to give

$$p_{bp} = p - p_{bw} - \frac{\sigma_{\theta cp}^{(n)} t_c}{R} \tag{A3}$$

and hence

$$p_b = p_{bw} + p_{bp} \tag{A4}$$

However, the thin-walled cylinder equations are approximations to the exact solution, as given by Lame.[15] Although the error in p_{bp} is consistent with these approximations, typically less than a few percent, it has been found that under certain conditions considerable errors in the circumferential stress calculations can occur when using this estimated value for p_{bp}. If an error analysis is performed for the circumferential stresses σ_θ to assess the effects of small errors in p_{bp} on σ_θ (see Appendix B), the following relationship can be derived:

$$\frac{\Delta\sigma_\theta}{\sigma_\theta} = \Delta p_{bp} \Big/ \left[p_{bp} - p + \frac{p t_c}{R} \right] \tag{A5}$$

where $\Delta\sigma_\theta$ and Δp_{bp} are the respective errors in σ_θ and p_{bp}. For a thin-walled cylinder circumferentially reinforced with a fiber overwind, the interface pressure p_{bp} can approach the internal pressure p, resulting in the equation

$$\frac{\Delta\sigma_\theta}{\sigma_\theta} = \frac{R \Delta p_{bp}}{t_c p_{bp}} \tag{A6}$$

From this equation it is evident that when p and p_{bp} are approximately equal, the relative error in σ_θ is proportional to the relative error in p_{bp}, with the constant of proportionality given by R/t_c. Since for thin-walled cylinders R/t_c is typically greater than ten, it follows that small errors in the interface pressure predictions can induce large errors in the circumferential stress calculations.

If the interface pressure is significantly different from the internal pressure, as is the situation during winding, the relative errors in the interface pressure predictions are comparable with those of the circumferential stress calculations. It is for this reason that it is admissible to use the thin-walled cylinder approximations to calculate p_{bw}, i.e., Eq. (A2).

In view of the previous discussion, it is essential, therefore, that the pressure-induced interface pressure p_{bp} is evaluated using the Lame equations. Omitting details, it can be easily shown from a compound cylinder analysis that the required interface pressure p_{bp} is obtained from

$$p_{bp} = p \left[\frac{2R_i^2}{E_c(R_b^2 - R_i^2)} + \frac{\nu_c(R_i^2 - R_e^2)}{E_c(R_b^2 - R_i^2)} \right] \div \left[\frac{(R_b^2 + R_i^2)}{E_c(R_b^2 - R_i^2)} + \frac{(R_o^2 + R_b^2)}{E_f(R_o^2 - R_b^2)} \right] \tag{A7}$$

where R_i and R_b are the internal and interface radii, respectively, of the metallic case and R_o is the external radius of the fiber-reinforced metallic rocket motor (i.e, $R_o = R_b + nt_f$).

Appendix B: Error Analysis

The Lame equation for the circumferential stress at the outer surface of an internallly and externally pressurized cylinder of inner radius R_i and outer radius R_b is given by[15]

$$\sigma_\theta = -p + (p - p_{bp}) \left[\frac{R_b^2 + R_i^2}{R_b^2 - R_i^2} \right] \tag{A8}$$

where p and p_{bp} denote the internal and external pressures, respectively. If the internal pressure is assumed fixed but p_{bp} is subject to some small error Δp_{bp}, it follows from Eq. (A8) that the corresponding error in σ_θ, i.e., $\Delta\sigma_\theta$, is

$$\Delta\sigma_\theta = -\Delta p_{bp} \left[\frac{R_b^2 + R_i^2}{R_b^2 - R_i^2} \right] \tag{A9}$$

The preceding error can now be assessed relative to the actual stress by dividing Eq. (A9) by Eq. (A8) to give

$$\frac{\Delta\sigma_\theta}{\sigma_\theta} = \left\{ -\Delta p_{bp} \left[\frac{R_b^2 + R_i^2}{R_b^2 - R_i^2} \right] \right\} \div \left\{ -p + (p - p_{bp}) \left[\frac{R_b^2 + R_i^2}{R_b^2 - R_i^2} \right] \right\} \tag{A10}$$

Introducing the thin-walled cylinder approximation

$$\frac{R_b^2 + R_i^2}{R_b^2 - R_i^2} \doteq \frac{R}{t_c} \tag{A11}$$

reduces Eq. (A10) to the simple form

$$\frac{\Delta\sigma_\theta}{\sigma_\theta} = \Delta p_{bp} \Big/ \left[p_{bp} - p + \frac{t_c p}{R} \right] \tag{A12}$$

From Eq. (A12), the effect of errors in p_{bp} on σ_θ can be easily assessed. If the difference between p_{bp} and p is large, then the relative error in σ_θ is comparable with the relative error in p_{bp}. On the other hand, if p_{bp} equals p, then the relative error in σ_θ becomes proportional to the relative error in p_{bp}, with the constant of proportionality given by R/t_c. Since for thin-walled cylinders R/t_c will always be significantly greater than unity, the relative error in σ_θ for a small error in p_{bp} can become large.

Acknowledgments

The authors would like to acknowledge the contributions of Professor P. Stanley (Simon Engineering, University of Manchester, U.K.) who has been involved in the development of the work detailed in this paper and for the drafting of section IIIB. The authors would also like to acknowledge F. Phillis of Stress Engineering Services Ltd., whose photoelastic stress results were used in the preparation of this paper. Technical discussions with Messrs. Cook and Parratt at RARDE Waltham Abbey are also gratefully acknowledged.

References

[1]Cook, J. and Howard, A., "A Compact Hoop Test for Determining the Creep and Static Fatigue of Nominally Elastic Fibres and Rings," Conference on Fatigue and Creep of Composite Materials, 3rd International Conference on Metallurgy and Material Science, Roskilde, Denmark, 1982.

[2]Cook, J. and Howard, A., "Creep and Static Fatigue of Aromatic Polyamide Fibres," Conference on Fatigue and Creep of Composite Materials, 3rd International Conference on Metallurgy and Material Science, Roskilde, Denmark, 1982.

[3]Cook, J., "Tensile Strength Testing and Quality Control Procedures for Aromatic Polyamide Yarns," TECQ Conference, University of Surrey, England, 1984.

[4]*Groves, A., Margetson, J., and Stanley, P., "Stress Analysis of Fibre-Reinforced Metallic Rocket Motor Cases," unpublished MOD(PE) report, 1982.

[5]Stanley, P., Margetson, J., and Groves, A., "Analytical Stress Solutions for Fibre-Reinforced Metallic Rocket Motor Cases," *International Journal of Mechanical Science*, Vol. 26, No. 2, 1984, pp. 119–130.

[6]Margetson, J., Groves, A., and Stanley, P., "Stress Analysis of Metallic Rocket-Motor Cases Reinforced with a Viscoelastic Fibre Overwind," *International Journal of Mechanical Science*, Vol. 27, No. 7/8, 1985, pp. 439–452.

[7]*Grovers, A, Margetson, J., and Stanley, P., "Nomographic Design Procedures for Fibre-Reinforced Metallic Rocket Motor Cases," unpublished MOD(PE) report, 1986.

[8]Margetson, J., "Stress Analysis Procedures for the Design of Fibre-Reinforced Metallic Rocket Motor Cases," AIAA Paper 83-1330, June 1983.

[9]*Thorpe, T. E. and Stanley, P., "Stress Analysis of Rocket Nozzles with Integral Cylindrical Portion," Mechanical Engineering (MOD) Report, Manchester University, England, Aug. 1984.

[10]Scheid, F., *Numerical Analysis*, Schaums Outline Series, McGraw-Hill, New York, 1968.

[11]Zienkiewicz, O. C., *The Finite Element Method*, 3rd ed., McGraw-Hill, London, 1977.

[12]Frocht, M. M., *Photoelasticity*, Vols. 1 and 2, Wiley, New York, 1941.

[13]Durelli, A. J. and Riley, W. F., *Introduction to Photomechanics*, Prentice-Hall, Englewood Cliffs, NJ, 1965.

[14]Stanley, P., "Three-Dimensional Photoelastic Stress Analysis; Techniques and Applications," *Experimentelle Technik der Physik*, Vol. 16, 1968, pp. 201–216.

[15]Tomoshenko, S. and Goodier, J. N., *Theory of Elasticity*, 3rd ed., McGraw-Hill, New York, 1970.

*Request Ref. through first author's establishment.